The Metering Function in Centrifugal Microfluidic Systems: From Comparative Analysis to Design Guidelines

Ali Gholizadeh*, Olivier Verlaine, Tristan Gilet

Department of Aerospace and Mechanical Engineering, Microfluidics Laboratory, University of Liège, Liège, 4000, Belgium

Email: ali.gholizadeh@uliege.be

Abstract

Metering (also known as aliquoting) is a critical function in centrifugal microfluidic systems, enabling the division of a larger inlet volume into smaller, well-defined downstream volumes. However, existing metering techniques often face challenges related to accuracy, reproducibility, and adaptability to varying fluid volumes, geometric layouts, and operational conditions. In this study, we systematically investigate the metering process by characterizing its performance with respect to key parameters: inlet volume, rotational speed, chamber geometry, and the formation of liquid plugs. Extensive experiments were conducted using two distinct microfluidic configurations, each designed to evaluate metering performance across nano- and microliter scales. Comparative analysis of the designs revealed critical dependencies between metering accuracy and structural features, such as circuit architecture and surface wettability. Liquid plugs within geometries connected to the metering chamber were analyzed both experimentally and theoretically. A critical threshold in plug length and centrifugal acceleration was identified, above which plugs were consistently displaced. Additionally, we examined the influence of in-plane circuit layout by comparing chips patterned in either Cartesian or cylindrical coordinates. Systematic differences in metering precision and reproducibility were observed, arising purely from geometric alignment relative to the centrifugal force. This work establishes a comprehensive framework for optimizing the metering functionality in centrifugal microfluidics. It offers practical design guidelines for the development of robust Lab-on-a-Disk systems.

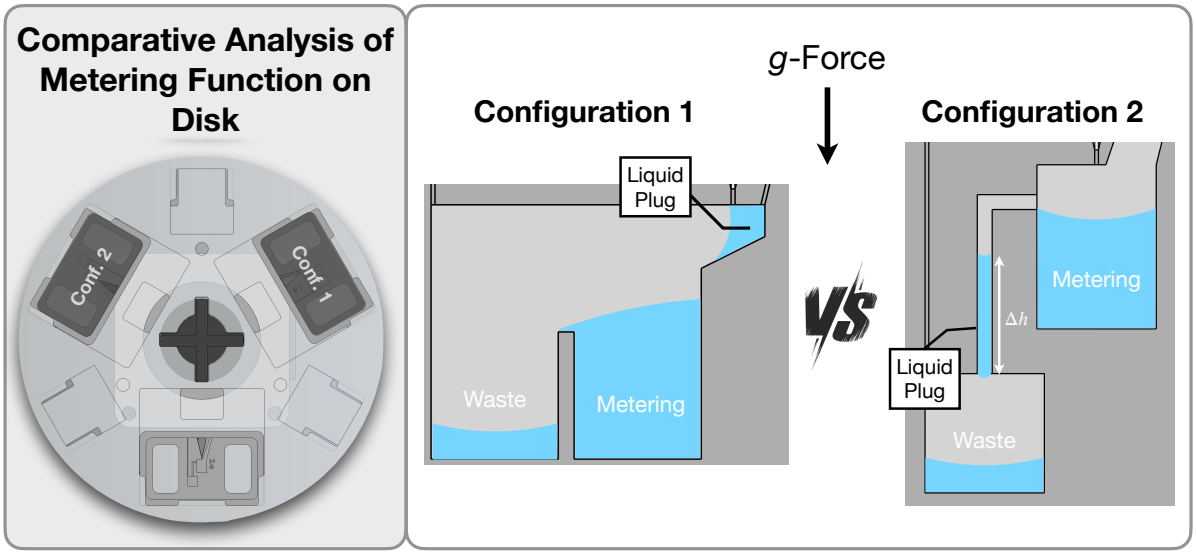

1 Introduction

Centrifugal microfluidic systems have emerged as powerful technologies for point-of-care diagnostics, biochemical analysis and sample preparation [1–4]. With minimal instrumentation, liquid samples ranging from nanoliters to milliliters can be manipulated radially outward within microfluidic circuits integrated into a rotating platform. This platform is typically designed as a monolithic disk, commonly referred to as a Lab-on-a-Disk (LOAD) [5]. Unlike pressure-driven Lab-on-a-Chip systems requiring external pumps [6,7], centrifugal platforms achieve controlled liquid manipulation solely through rotational accelerations. However, the monolithic nature of the LOAD design limits flexibility and increases the upfront costs for prototyping, particularly in limited R&D settings. Chip-on-a-Disk (COAD) systems, which consist of microfluidic chips simply inserted into a reusable disk structure, offer strongly reduced prototyping costs and enable the testing of a large number of microfluidic designs [8]. By precisely adjusting the rotational speed, fluid movement can be dynamically regulated, enabling a range of unit operations such as mixing, separation, and metering, which is critical to quantitative assay performance. To ensure accurate, autonomous workflows, careful engineering and predictive modeling of these fluidic processes are essential [9].

Metering, or aliquoting, is the process of dividing a larger liquid sample into smaller, well-defined sub-volumes. Metering strategies are broadly categorized into one-stage and two-stage approaches. In one-stage methods, the metering occurs directly in the final readout chamber [10]. This approach offers design simplicity and is well-suited for applications in chemical analysis [11], but it is limited to processing a single liquid, making it unsuitable for workflows involving mixing [12] and/or separation [13]. In contrast, two-stage methods allow further processing in a chamber downstream of the metering unit. However, this approach requires more complex designs, as microvalves [14] are often essential for controlling the precise transfer of liquid into subsequent chambers [15,16]. These valves—whether passive (e.g., capillary [17] and siphon [18] valves) or active (e.g., magnetic valves [19])—directly impact metering accuracy. Their performance depends on several parameters, including burst pressure thresholds, rotational speed, and actuation timing. Untimely valve triggering or unintended leakage can result in incomplete or excessive liquid transfer [20].

Accurate metering is therefore a key requirement across many centrifugal microfluidic applications. In enzymatic and immunoassays, precise reagent volumes determine reaction kinetics and signal intensity, directly affecting assay sensitivity and reproducibility [21,22]. In dilution workflows, defined volume ratios set the final analyte concentration, while in sample preparation modules, consistent aliquoting ensures reliable downstream processing [23]. Several metering functions can be processed in parallel by integrating multiple circuits within a single microfluidic chip or disk, enabling high-throughput and/or multiplexed assays [24]. In these systems, liquid samples are typically distributed into one or more defined sub-volumes before transfer to reaction chambers or processing units [25]. The reliability of these operations depends strongly on the geometry of the metering unit and in-plane circuit layout. Microfluidic circuits are most commonly implemented in cylindrical layouts [16,26,27], in which geometrical features are aligned with the radial direction of the centrifugal force. However, different applications may impose additional design constraints, including compatibility with standard centrifuges [28]. For example, Cartesian layouts are well suited for microfluidic designs that mimic well-plate formats used in swinging-bucket centrifuges [29]. These layouts introduce angular misalignment with the centrifugal force, which can alter flow paths and metering behavior. Despite their growing relevance in prototyping and modular platforms [30], the impact of such geometric offsets on metering accuracy and reproducibility has not been systematically investigated.

To date, previous studies have demonstrated precise metering (coefficients of variation below 5%) in dedicated assays within LOAD platforms (e.g., [11,31,32]). In particular, Mark et al. [31] and Schwemmer et al. [33] established quantitative design rules for centrifugo-pneumatic metering, in

which the metered volume is defined by enclosed chamber geometries and compressed air volumes. While these approaches enable highly accurate volume definition, they are intrinsically limited to closed pneumatic systems and specific operating conditions. Lutz et al. [32] investigated capillary-controlled metering and overflow concepts, highlighting the influence of geometry and wetting on metering performance. However, their analysis focused on specific valve architectures and did not investigate the combined effects of inlet volume, residual liquid retention, or layout-induced force misalignment. Despite these advances, the metering performance can remain sensitive to dynamic operational conditions where capillary and inertial forces are in challenge at the liquid–air interface. Rotational speed controls the centrifugal acceleration, directly influencing fluid displacement and interface positioning [34,35]. The inlet volume, which sets the available fluid head prior to metering, was previously reported to have a negligible effect when varied by ± 10% [33], yet its influence in open and overflow-based metering architectures remains poorly characterized. Fabrication methods and chamber manufacturing tolerances have also been shown to affect metered volume [4,31]. In multi-step workflows, cumulative over-metering can arise from residual liquid trapped in narrow interconnecting channels [32], while surface wettability may promote parasitic liquid plugs or incomplete sample displacement, particularly in confined geometries [32,36]. Although qualitative design recommendations—such as modifying junction geometries to interrupt undesired liquid connections—have been proposed [37], a systematic framework linking kinematic and geometric parameters to metering accuracy across different architectures and layouts is still lacking.

In this study, we present a comparative investigation of the metering function across different microfluidic configurations and operational conditions using a flexible COAD platform. We report experimental measurements and provide physical interpretations of the observed behaviors. Key parameters influencing metering accuracy—including chamber geometry, rotational speed, inlet volume, and surface wettability—are identified and evaluated. Special attention is given to two distinct configurations, where discrepancies between expected and actual metered volumes are analyzed in detail. Furthermore, we investigate the effect of in-plane circuit arrangement by comparing chips with Cartesian versus cylindrical offsets, revealing systematic differences in metering accuracy and reproducibility that arise solely from layout geometry. The findings offer practical design guidelines and predictive tools for improving metering functionality and precision in future centrifugal microfluidic platforms.

2 Material and Methods

2.1 Microfluidic Chips: Design, Fabrication, and Materials

Microfluidic chips were designed in two configurations *1* and *2* using SolidWorks, and fabricated with 3D printing resin (Detax MedicalPrint, clear-04016) at the Sirris research center. Adhesive tape (Labelor, 3635E5-38B297) was used to seal the microfluidic circuit. The advancing and receding contact angles were measured for DI water on resin ($\theta_a = 89°$, $\theta_r = 57°$) and tape ($\theta_a = 102°$, $\theta_r = 72°$). Each chip had a rectangular shape, 40 mm long, 5.5 mm thick, and 24 mm wide, with a single microfluidic circuit on its surface. This circuit included a pyramidal inlet well with a square cross-section of area 9 mm^2 at the inlet and 0.01 mm^2 at the outlet, and identical across all designs. A metering chamber was placed downstream of the well, with its depth (H) being the smallest dimension. A waste chamber was positioned adjacent to the metering chamber to collect the excess fluid. The fluid gated to the waste chamber either by stepping over a thin wall separating both chambers (Configuration *1*, Figure 1a, top) or by penetrating into a narrow connecting channel (Configuration *2*, Figure 1a, bottom). Five different designs (see Supporting Information for details) were considered for each configuration. Each design was tailored to evaluate the metering function under specific conditions, for example with two different metering chamber volumes, 5.12 µL and 0.64 µL.

Two additional chips were fabricated, each comprising three microfluidic circuits arranged either in a Cartesian (offset by 9 mm) or a cylindrical layout (offset by 15°) (Figure 1c). Each circuit included microfluidic units with identical dimensions to those described for configuration *2*. The metering chamber volume was 0.64 µL.

2.2 Experiments

The microfluidic chips were set up in a Chip-on-a-Disk (COAD) format: they were inserted into a horizontal disk spinning about a vertical axis (Figure 1b). The microfluidic features were also in a horizontal plane, with the metering chamber at 5 cm from the disk axis. A centrifugal bench was built to control the disk rotation. The rotational speed could reach up to 3000 rpm, corresponding to a maximum centrifugal acceleration of 504 *g* at the outermost radial position of the metering chambers. The bench comprised a computer-controlled stepper motor connected to a vertical shaft upon which the disk was mounted. A high-speed Photron AX50 camera, equipped with a Zeiss Milvus 2/100M macro lens, enabled top-view, real-time monochromatic imaging of the microfluidic chip and the fluids therein once per rotation. The video resolution was between 21 µm and 56 µm per pixel, depending on the experiment. The exposure time was set to 1 µs, resulting in a motion blur of 15 µm at the highest radial position of the microfluidic chambers. In some experiments, post-metering images were taken using a Canon 250D camera coupled with an MP-E 65 mm macro lens, providing higher resolution (2 µm per pixel) and full-color images.

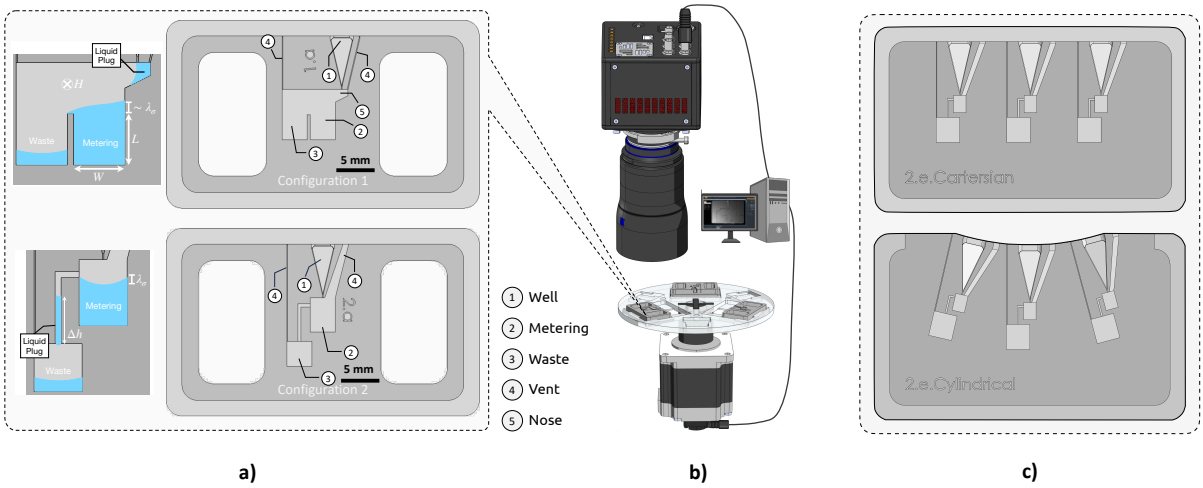

Figure 1: (a) Chip architecture for configurations 1 (top) and 2 (bottom). Each chip comprises an inlet well (1), a metering chamber of dimensions $W \times L \times H$ (2) and a waste chamber (3). The chambers are successively visited by the liquid samples. Metering and waste chambers are vented (4). A zoomed schematic is provided next to each configuration, showing the liquid within the corresponding fluidic units. The meniscus rise or depression in the top of metering chamber is represented at the scale of λ_σ, and liquid residues are illustrated as liquid plugs in the nose region and in the waste channel with height Δh. (b) Experimental setup, comprising a horizontal Chip-on-a-Disk platform mounted on a vertical-axis stepper motor, and a high-speed camera positioned to record a top view of the disk. In (b), the chips are positioned such that the radially outward direction of disk, namely the direction of the centrifugal force, corresponds to the downward direction in (a). (c) Two microfluidic chips designed with three circuits in Cartesian (top) and cylindrical (bottom) layouts. (a) and (c) are in the same scale.

2.3 Chip Preparation and Testing

The microfluidic chips were cleaned after each experiment by successively rinsing with isopropanol and DI water, then drying with compressed air. To evaluate the metering function of chambers of volume 5.12 µL, three different liquid volumes were dispensed in the inlet well: 7 µL, 8 µL, and 9 µL. They are later referred to as the inlet volumes. After dispensing the liquid into the well, centrifugation was initiated at 250 rpm for 5 seconds. The rotational speed was then ramped up to the burst

frequency of 1100 rpm, overcoming capillary forces at the well outlet to allow liquid invasion into the metering chamber. This burst frequency was maintained for less than 250 ms. Right after bursting, the speed was set to a fixed running speed ranging from 500 rpm to 2250 rpm, with increments of 250 rpm applied either within the same experiment or across separate experiments. This process was repeated for all tested inlet volumes, and a cleaning step was consistently performed after each experiment. Microfluidic chips with metering chambers of volume 0.64 µL were also evaluated using inlet volumes of 1 µL, 2 µL and 3 µL, which correspond to burst frequencies of 1500 rpm, 1300 rpm and 1200 rpm, respectively.

2.4 Data Analysis

For single-circuit chips, a video of each metering event was recorded and analyzed. When metering was successfully achieved, the metered volume was quantified using image processing in MATLAB. The associated error on volume measurement was primarily due to the limited resolution, i.e., the finite size of pixels. In the present videos, it was always less than 4% of the metered volume. An ANOVA test was also performed in MATLAB to determine which parameters significantly affected the metered volume. For three-circuit chips, an image was captured after each experiment and analyzed via image processing in Python. This allowed an automated measurement of the metered volumes, with an estimated error within ±2%.

2.5 Analysis of Liquid Plugs

Metering was considered inaccurate when liquid plugs remained at undesired locations, as they would possibly join the metered volume during subsequent microfluidic operations. When such plugs were observed, their height was manually measured using ImageJ. From a theoretical perspective, such a liquid plug can be approximated as a liquid column of height Δh. This plug is subjected to the centrifugal acceleration, given by

$$g^* = \bar{r}\,\Omega^2, \qquad \text{(Eq. 1)}$$

where Ω is the rotational speed and $\bar{r}$ is the average radial distance from the axis of rotation. The resulting centrifugal pressure p_c acting on the liquid column is

$$p_c = \rho\, g^* \Delta h, \qquad \text{(Eq. 2)}$$

where ρ is the liquid density (997 kg/m^3 for water). Most circuits of configuration *2* were designed in a Cartesian layout, so the centrifugal acceleration was not strictly aligned with the plugs in the waste channel. Nevertheless, this angular deviation was always less than 6° and it was neglected in the calculation of p_c.

Conversely, the capillary pressure p_σ that the plug interfaces may sustain without sliding is estimated as

$$p_\sigma = k\frac{2\sigma}{H}\,, \qquad \text{(Eq. 3)}$$

where k is a dimensionless curvature factor, σ is the liquid surface tension (0.073 N/m for water) and H is the smallest dimension of the geometry—here, the depth of the microchannel (e.g., $H = 100$ µm in waste channel) or chamber. The curvature factor k, which accounts for the influence of contact angle hysteresis [36], is typically on the order of unity. Herein, we assume $k = 1$.

As long as the plugs remain stationary within the microfluidic features, their interfaces are in hydrostatic equilibrium state, with centrifugal and capillary pressures balanced. Therefore, the upper

bound on the capillary pressure yields the maximum height a liquid plug can reach while remaining motionless,

$$\Delta h < \Delta h_{\max} = k\frac{2\lambda_\sigma^2}{H}, \qquad \text{(Eq. 4)}$$

where the capillary length λ_σ is defined as

$$\lambda_\sigma = \sqrt{\frac{\sigma}{\rho g^*}}. \qquad \text{(Eq. 5)}$$

3 Results and Discussion

3.1 Phenomenology

Figure 2a presents the metering achieved in configuration *1* by Design 1.a. An initial volume of 8 µL of water was pipetted into the well, the capillary valve was burst, and then steady centrifugation at 750 rpm (30 g where g = 9.8 m.s^{-2}) transferred the liquid into the metering chamber (t = 13 s). The nose feature forced the liquid to systematically attach to the right sidewall when progressing towards the metering chamber [38], ensuring a void-free filling as well [39]. Once the metering chamber was filled, excess liquid was gated to the waste chamber on its left. A thin wall separating the metering and the waste chambers enabled metering at very low frequencies (e.g., 750 rpm). Consequently, it took t = 45 s to transfer all the residual liquid from the nose and complete metering. At hydrostatic equilibrium, the liquid–air interface was positioned on average approximately 0.4 mm above the height of the thin wall (over-metering). Under these operating conditions, the effective capillary length was $\lambda_\sigma \approx 0.49$ mm, which was of the same order of magnitude as the observed meniscus (de Gennes et al. [40]). The upward shift of the interface relative to chamber volume ($V_{\text{measured}} - V_{\text{chamber}} = \Delta V > 0$) increased the retained liquid volume in the metering chamber, resulting in a maximum relative over-metering approximately 10% larger than the ideal geometric prediction ($\Delta V \sim 10\%\ V_{\text{chamber}}$).

Figure 2b illustrates the metering process achieved in configuration *2* by Design 2.a. Similarly, an initial volume of 8 µL of water was pipetted into the well and the capillary valve was burst. Upon steady centrifugation at 1000 rpm the liquid began filling the metering chamber. Here, the well outlet was directly connected to the metering chamber (i.e., there was no nose in this design), allowing metering to complete in t = 11 s. At this speed and under quasi-static equilibrium, the liquid–air interface inside the metering chamber remained approximately 0.2 mm below the top of the chamber—opposite to the upward rise observed in configuration 1, leading here to under-metering ($\Delta V < 0$). The corresponding capillary length ($\lambda_\sigma \approx 0.36$ mm) was comparable to this downward shift of the meniscus. The missing volume represented roughly 2% of the chamber volume. Additionally, the metering process led to the formation of a liquid plug of height Δh = 2.3 mm within the waste channel. This plug was smaller than the maximum liquid plug height $\Delta h_{\max}$ = 3.33 mm at 1000 rpm (45 g). The rotational speed was then gradually increased. The liquid plug was fully removed at 3000 rpm (402 g), when $\Delta h_{\max}$ had decreased to 0.37 mm.

In all the present experiments, the maximum velocity v of the interface in the vicinity of the metering chamber was observed to be lower than 10 mm/s. This upper bound allows us to estimate the importance of inertia and viscous shear in the determination of the metered volume. The ratio of inertial pressure ρv^2 to capillary pressure σ/H is expressed by the Weber number $We = \rho v^2 H/\sigma < 7 \times 10^{-4}$ for H = 0.5 mm. Since $We \ll 1$, inertial forces are not likely to play any significant role in

the determination of the metered volume. Similarly, the relative importance of viscous shear $\mu v/H^2$ (where $\mu \approx 10^{-3}$ Pa.s is the dynamic viscosity of water) and capillary pressure gradients $\sigma/(WH)$ is a modified capillary number $Ca^* = \mu v W/(\sigma H) < 9 \times 10^{-4}$ for $W = 3.2$ mm. Since $Ca^* \ll 1$, viscous shear is not expected to influence the metered volume either. Consequently, the metered volume is solely determined by the competition between centrifugal and capillary forces, which is represented by the ratio between the characteristic lengths of the metering chamber and the capillary length λ_σ.

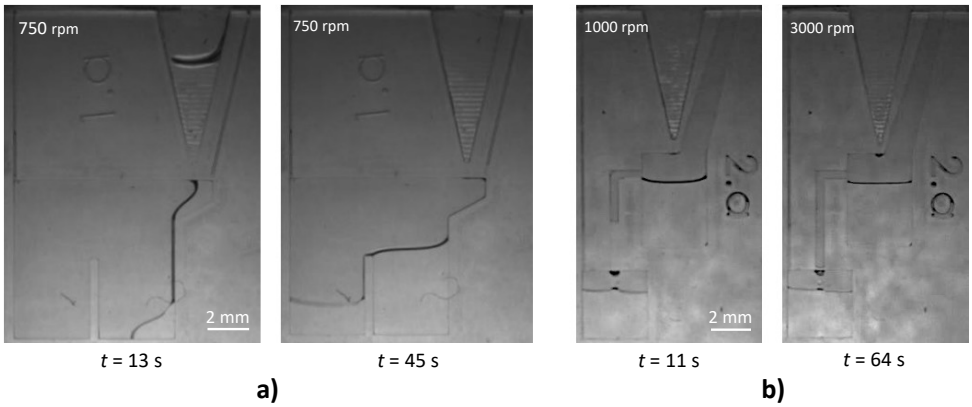

Figure 2: (a) Configuration 1, Design 1.a – Upon centrifugation at 750 rpm, the liquid smoothly entered the metering chamber from the well (t = 13 s). The metering process was completed in t = 45 s. (b) Configuration 2, Design 2.a – Upon centrifugation at 1000 rpm, metering was completed in t = 11 s, although a 2.3 mm-high liquid plug remained in the waste channel. Increasing the centrifugation speed to 3000 rpm subsequently flushed the liquid plug into the waste chamber (t = 64 s). In both configurations, the inlet volume was 8 µL. The corresponding videos are available in the Supporting Information.

3.2 Volume Analysis upon Metering Function

To evaluate the metering function under varying operational conditions, a series of experiments were conducted across different inlet volumes, rotational speeds, and microfluidic designs (a-e) (See raw datasets in the Supporting Information). In Figure 3, the normalized volume variation $(V_{\text{measured}} - V_{\text{chamber}})/(WH\lambda_\sigma)$ is plotted against the dimensionless ratio H/λ_σ, which varies with rotational speed through its dependence on the capillary length. This representation captures how much the liquid–air interface deviates from the chamber geometry in units of the capillary length and therefore directly reflects the magnitude of capillary-induced interface displacement relative to centrifugal forcing. Across all designs and operating conditions, the normalized deviation remains on the order of unity ($\Delta V/(WH\lambda_\sigma) \sim 1$), indicating that the interface rise or depression inside the chamber consistently scales with λ_σ. In both configurations, Design 1.b (triangles in Figure 3)—featuring a low-aspect-ratio metering chamber ($W \ll L$)—displayed distinctly different behavior from the other designs, exhibiting the largest scatter across inlet volumes. By contrast, the remaining designs, which had chamber aspect ratios close to or larger than unity, produced configuration-specific but consistent metering behavior.

In configuration *1*, the metered volumes were generally overestimated across most conditions, with the overestimation being pronounced for Design 1.e (circles in Figure 3, left), which had the smallest metering chamber (0.64 µL) (dispensed volume from 1 µL to 3 µL). An ANOVA for $N = 54$ independent measurements confirmed that both the inlet volume (F-value $F(4, 38) = 6.6$, p-value $p = 4 \times 10^{-4}$) and design variation ($F(3, 38) = 3.24$, $p = 0.0327$) significantly affected metering performance, whereas the rotational speed did not have a statistically significant influence ($F(7, 38) = 2.21$, $p = 0.055$). Importantly, Design 1.e—whose chamber width is roughly half that of the other designs—showed heightened sensitivity to metering volume variations at lower rotational speeds. As the rotation speed decreases, the capillary length increases and becomes comparable to the smaller chamber width and depth

($\lambda_\sigma \sim W, H$). Under these conditions, capillary effects dominate over centrifugal forces, resulting in larger interface curvature and therefore greater susceptibility to volume variation.

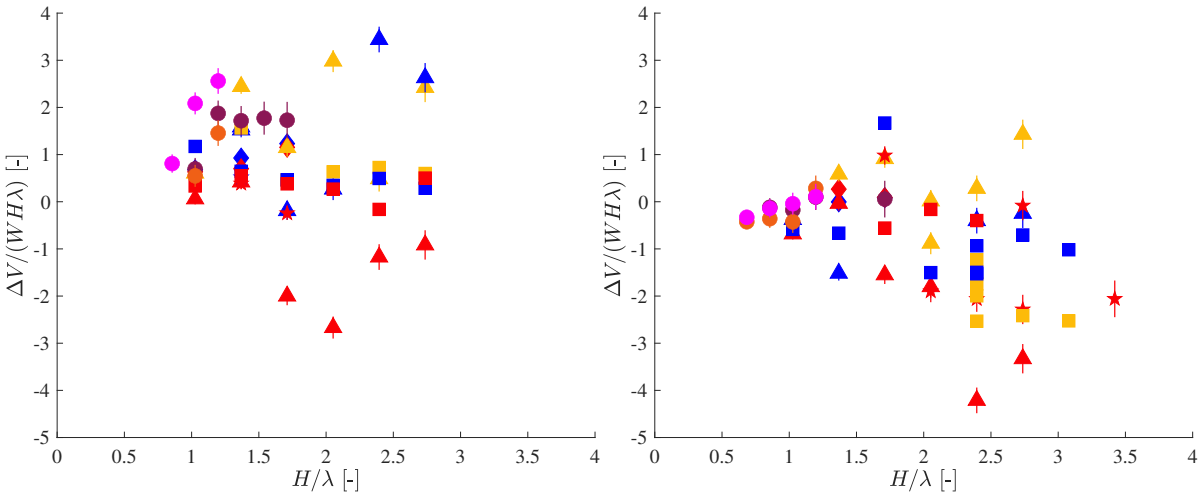

Figure 3: Normalized metering volume variation across different rotational speeds for five design variants – a (diamond), b (triangle), c (star), d (square), e (circle) – in configurations 1 (left) and 2 (right). Each color represents a specific inlet volume: 1 µL (red), 2 µL (orange), 3 µL (magenta), 7 µL (green), 8 µL (dark blue), 9 µL (light blue). Error bars correspond to the pixel size. The corresponding table of data is available in the Supporting Information.

On the other hand, for configuration *2*, the metered volumes were consistently underestimated across all designs with most of the inlet volumes. An ANOVA for $N = 57$ individual measurements indicated that only design variation had a significant impact on metering performance ($F(3, 40) = 9.84$, $p = 1 \times 10^{-4}$), whereas neither inlet volume ($F(4,40) = 0.41$, $p = 0.7989$) nor rotational speed ($F(8,40) = 0.26$, $p = 0.9741$) had significant effects. Specifically, Designs 2.c (stars in Figure 3, right) and 2.d (squares in Figure 3, right) yielded lower volume ratios. Therefore, additional experiments were conducted on Design 2.d to elucidate the mechanism behind this reduction in metered volume, as illustrated in Figure 4. Initially, 7 µL of DI water was dispensed into the well. Upon centrifugation at 2250 rpm, the liquid entered the metering chamber (t = 7.33 s), after which excess liquid overflowed into the waste chamber (t = 7.91 s), marking the apparent completion of metering. However, closer inspection revealed the presence of a thin liquid rivulet that persisted on the right side of the channel between metering and waste chambers. This rivulet permitted unintended liquid drainage from the metering chamber (t = 8.58 s). Although the images did not clearly show whether the rivulet extended along two or three channel walls, this observed drainage flow differed from a capillary corner flow, as the Concus-Finn condition [41,42] was not satisfied: the walls were printed at 90° and both water-resin and water-tape contact angles exceeded 45°. Instead, the rivulet flow was driven by the centrifugal force and potentially influenced by surface heterogeneities or resin residues remaining from the printing process, which may have locally altered wettability. Top-view snapshots proved insufficient to clearly explain the flow mechanism. Nevertheless, closer observation disclosed a liquid film (thin dark line) along the right wall of the waste channel at t = 7.91 s, which became thicker and more pronounced at t = 8.58 s, when droplet formation was observed—confirming flow along the wall. This liquid film then gradually thinned and became less visible, correlating with the temporal evolution of drainage (t = 8.58 s – 55.95 s) and eventually breaking up at t = 64.35 s, possibly due to film instability along the wall surface [43]. The overall reduction in metered volume caused by this drainage was 0.91 µL, suggesting either excessive retention or liquid loss driven by capillary and centrifugal forces.

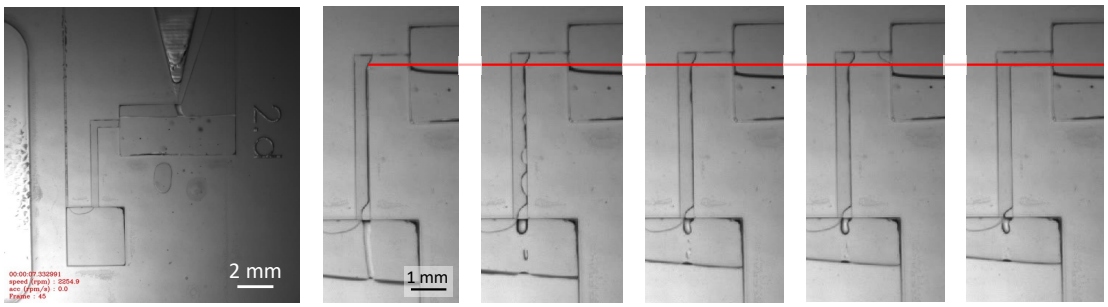

Figure 4: Time-sequence images showing some further emptying of the metering chamber happening in Design 2.d during centrifugation of 7 µL of liquid at 2250 rpm. Despite metering being apparently complete (t = 7.91 s), additional liquid continued to drain from the chamber for up to one minute, resulting in volume loss of 0.91 µL. The horizontal red line indicates the initial liquid level at the end of the metering step. The corresponding video is available in the Supporting Information.

3.3 Nose Issues with Configuration *1*

Figure 5 illustrates the metering achieved for Design 1.c after less than one minute of centrifugation at low rotational speed (500 rpm, i.e., 14 g). This capability to meter at low speed is critical for complex systems incorporating passive capillary valves [17,44], which require sequential valve bursting upon speed increases. However, residual liquid (~ 360 nL) was consistently observed within the nose region, posing a challenge for accurate metering. Equation 4 is not directly applicable to rationalize the existence of this residual volume in the nose, since it is not a liquid plug with upper and lower liquid-air interfaces. Nevertheless, its presence is not surprising: the effective capillary length ($\lambda_\sigma = 0.73$ mm at 500 rpm) is comparable to the characteristic dimensions of the residual liquid (~ 1.1 mm in height, 0.7 mm in width and 0.5 mm in depth), suggesting that capillary forces can counteract centrifugal forces and retain the residue.

This comparison establishes a practical design criterion: to avoid residual liquid, the characteristic dimensions of the nose must remain larger than the effective capillary length under operating conditions. Such control is particularly critical for LOAD applications requiring high metering accuracy, as even small residual volumes can compromise quantitative results. This is evidenced by recent work employing nose-shaped metering for enzymatic assay [38], where precise volume definition is essential for assay reliability.

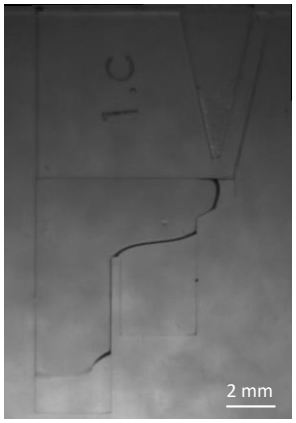

Figure 5: Metering was achieved with Design 1.c by centrifuging 9 µL of liquid at 500 rpm in less than a minute. However, a liquid residue was observed in the nose beneath the well outlet. The corresponding video is available in the Supporting Information.

3.4 Liquid Plug Issue within Configuration *2*

The presence of a liquid plug within the waste channel presents a critical bottleneck to accurate metering in centrifugal microfluidic systems, particularly in architectures designed for robust sample preparation that rely on chip reorientation to transfer liquid from the metering chamber to downstream units [8,30]. To further investigate this phenomenon, the height of the liquid plug Δh was measured at various rotational speeds for each design (See raw datasets in the Supporting Information). An upper bound for the theoretical plug height $\Delta h_{\max}$ was calculated using Eq. 4. As shown in the parity plot (Figure 6), all measured plug heights satisfied the condition $\Delta h < \Delta h_{\max}$. Plug heights within 7% of the $\Delta h_{\max}$ threshold were observed at all speeds except for 750 rpm, where the largest Δh was 4 mm while $\Delta h_{\max} \approx 5.5$ mm. This deviation likely resulted from a smaller dataset, as Δh was constrained by the total height of the waste channel in all designs except for Design 2.c.

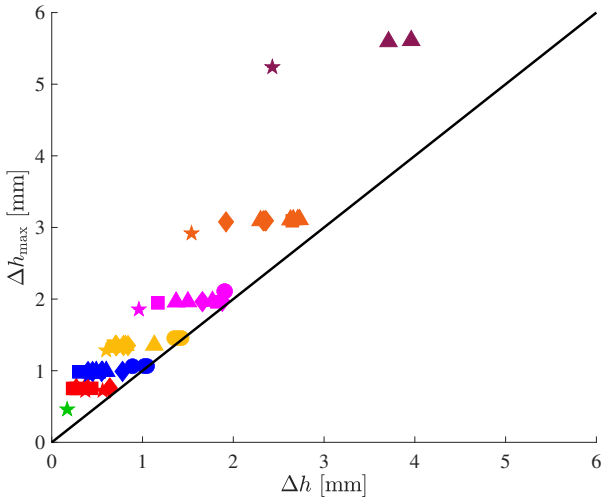

Figure 6: Parity plot comparing the measured liquid plug heights with theoretical predictions from Eq. 4, for five design variants – a (diamond), b (triangle), c (star), d (square), e (circle) – of configuration 2. Symbols in different colors represent various rotational speeds: 750 rpm (purple), 1000 rpm (orange), 1250 rpm (magenta), 1500 rpm (yellow), 1750 rpm (blue), 2000 rpm (red), and 2500 rpm (green). The error bar, corresponding to the pixel size, is smaller than the symbol size. The corresponding table of data is available in the Supporting Information.

3.5 Effect of Chamber Aspect Ratio on Metering Function

Wide metering chambers may be subjected to another issue: the inlet volume might not be sufficiently larger than the metering volume to establish a continuous liquid column from the upstream interface (at the inlet well) to the downstream interface (at the entrance of the waste channel). As a result, the generated centrifugal pressure may be insufficient to overcome capillary forces. To illustrate this, the metering function of Design 2.d ($V_{\text{chamber}} = 5.12$ µL), which had a W/L ratio of 4, is presented in Figure 7. Upon dispensing $V_{\text{inlet}} = 7$ µL of DI water and centrifugation at 500 rpm (14 g), a portion of the liquid remained in the inlet well, preventing perfect metering. When the rotational speed was increased to 1500 rpm (126 g), the liquid was entirely displaced from the inlet well to the metering chamber. The upstream liquid interface stabilized at $\Delta h = 0.16$ mm above the inlet of the waste channel. This liquid column height was smaller than the calculated threshold $\Delta h_{\max} = 0.24$ mm (Figure 7-inset). Therefore, the liquid in excess did not penetrate the waste channel, resulting in incomplete and inaccurate metering.

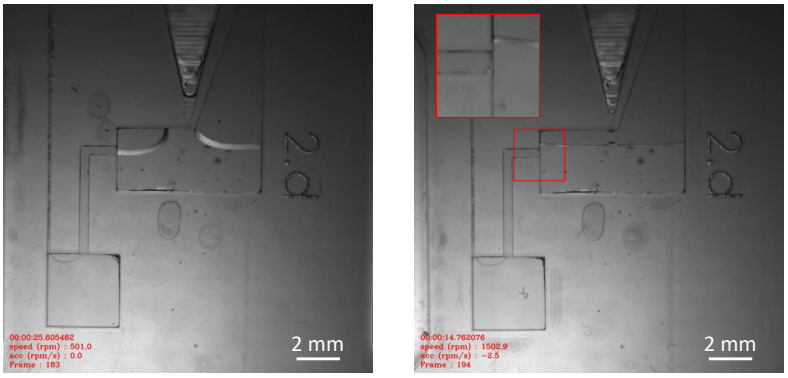

Ω =500 rpm Ω =1500 rpm

Figure 7: Upon dispensing 7 µL of DI water into the inlet well and centrifugation, incomplete metering was observed at 500 rpm (14 g) and 1500 rpm (126 g) due to insufficient centrifugal pressure. The inset shows the liquid meniscus in the waste channel. The corresponding videos are available in the Supporting Information.

3.6 Effect of Cartesian and Cylindrical Layouts on Metering Function

Centrifugal forces can act differently on circuits positioned with a Cartesian vs. cylindrical layout. This variation may significantly impact both metering accuracy and reproducibility. To analyze these effects, we conducted the metering experiments to 2.e.Cartesian and 2.e.Cylindrical chips and assessed reproducibility by repeating the experiments five times. In each experiment, 3 µL of blue-dye water was initially pipetted into the inlet well of each circuit. The chip was then centrifuged at 2000 rpm for 5 s, which was sufficient to complete metering. The rotational speed was then increased up to 3000 rpm for 5 s to remove the liquid plug in the waste channel. As shown in Figure 8a, the Cartesian layout resulted in an uneven distribution of the volume across three metering chambers. In this layout, the liquid-air interface aligns perpendicular to the local centrifugal acceleration. For the left and right chambers, this direction is not aligned with the chamber walls anymore. In the left chamber, the centrifugal force pushed the liquid toward the waste channel, whereas in the right chamber, it pushed the liquid against the opposite vertical wall—resulting in the smallest (519 nL) and largest (654 nL) metered volumes, respectively. This systematic asymmetry can be quantitatively estimated by considering the angular misalignment $\alpha = 15°$ between the chamber axis and the centrifugal acceleration (Figure 8a, inset). A simple geometric analysis yields a relative metering error

$$\frac{|\Delta V|}{V_{\text{chamber}}} \approx \frac{W\tan(\alpha)}{2L}, \qquad \text{Eq. 6}$$

which evaluates to approximately 8.8% for the present design. This predicted deviation is of the same order of magnitude as the experimentally observed coefficient of variation across the three metering chambers, indicating that a substantial fraction of the measured variability originates from deterministic geometric misalignment rather than stochastic experimental noise. Consistently, the metered volumes at each chamber position were highly reproducible across five repeated trials (CV $\leq$ 5%), confirming that the dominant contribution to the overall CV is systematic. By contrast, Figure 8b demonstrates consistent metering performance across the three chambers in cylindrical layout, with average CV $\leq$ 3% across five repeated trials. In this case, the chamber walls remained aligned with the centrifugal acceleration, minimizing interface tilting and eliminating layout-induced bias. Figure 8c thus highlights a clear and reproducible difference in metering performance (metering ratio = $V_{\text{measured}}/V_{\text{chamber}}$), arising purely from layout geometry.

Although both layouts are compatible with centrifugal microfluidic systems, Cartesian arrangements introduce predictable, position-dependent volume variations. These can be mitigated by intentionally compensating chamber volume (e.g., chambers situated to the left of the central metering unit—reflecting the position of the adjacent waste channel—should have slightly smaller volumes than those on the right side). Alternatively, if identical and parallel chambers must be featured across the layout, we recommend designing the chamber width W as the smallest chamber dimension and aligning the largest dimension such as depth H along the rotation axis (i.e., perpendicular to the disk plane), such that $W/H < 1$. Such design rules ensures that centrifugal acceleration remains effectively uniform across the larger chamber dimension, improving metering accuracy and reproducibility. This design consideration is especially important for precise dispensing and sample preparation based on centrifugation sequences, e.g., using standard centrifuges and well plates integrated with microfluidic modules to conduct enzymatic assays [45].

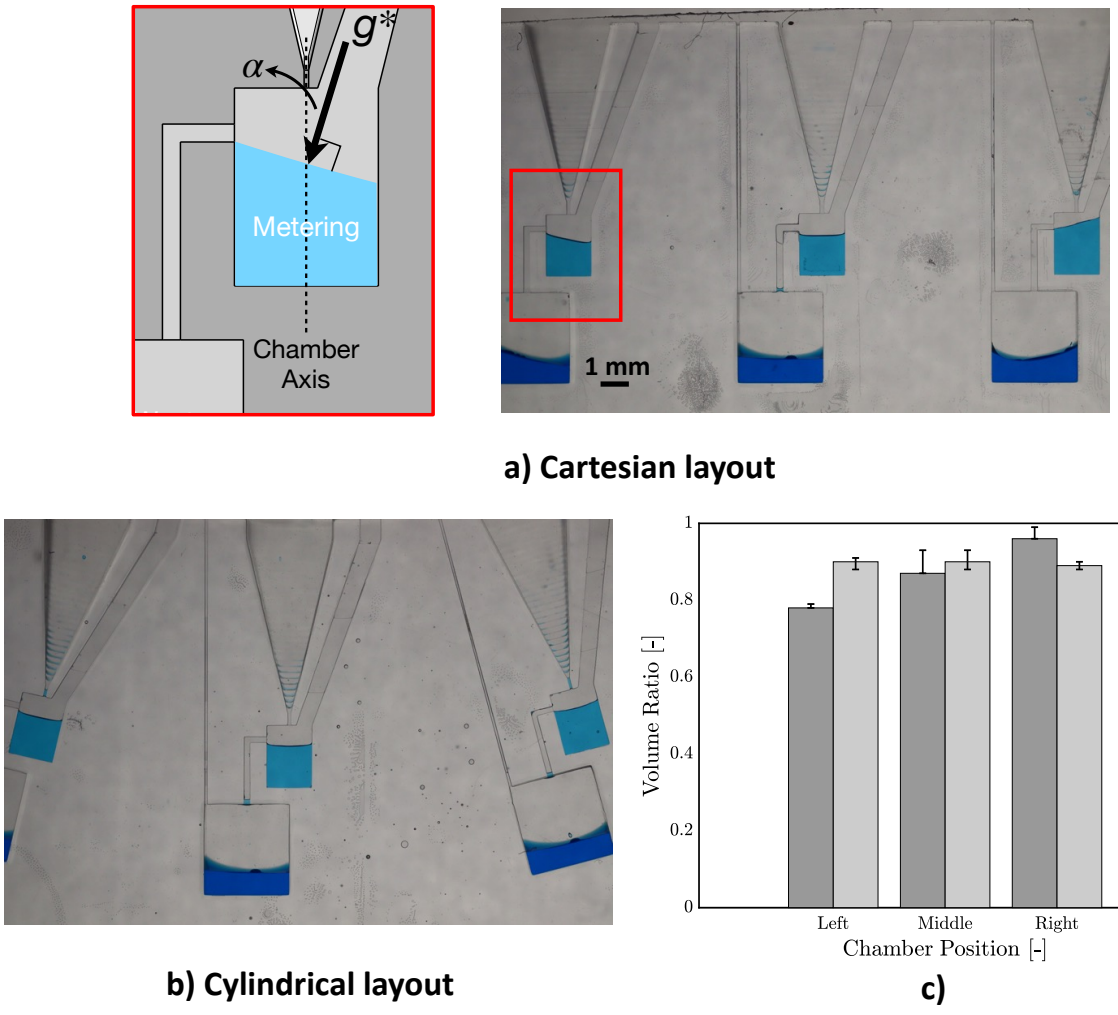

Figure 8: Comparison of the metering function in two microfluidic chips, each comprising three circuits arranged in either Cartesian or cylindrical layout. (a) In the Cartesian layout, with an offset of 9 mm between circuits, the metered volume increased for the chambers from left to right, yielding a CV of 12%. (b) In the cylindrical layout with an angular offset of 15° between circuits, the metered volumes were almost equal for all the chambers (CV = 3%). (c) The volume ratio for each chamber is shown for the Cartesian (dark grey bars) and cylindrical (light grey bars) layouts. Error bars indicate replicate measurements. The corresponding table of data is available in the Supporting Information.

3.7 Practical Design Guidelines for Reliable Metering

A central aim of this study was to move beyond qualitative observations and extract practical, quantitative design rules that can guide the development of reliable metering units in centrifugal microfluidic systems independent of a particular assay implementation. While individual effects—such as chamber geometry, inlet volume, capillary length, rotational speed or centrifugal acceleration g^*, and liquid-plug retention—have been reported separately in earlier works, no unified framework has been established to connect these factors into actionable design guidelines.

Here, we summarize the combined experimental and theoretical findings of this work into two Table 1 and Table 2. As prototyping can be costly and time-consuming, reliance on trial-and-error optimization is not recommended. Rather than prescribing fixed designs, these guidelines identify the governing mechanisms and failure modes that must be controlled to ensure reliable metering performance.

Table 1: Universal design rules for metering in centrifugal microfluidics.

Design Principle	Guidelines (Prescriptive DO/DO NOT)	Observed effect
A. Chamber aspect ratio (W/L)	DO target aspect ratio $W/L \approx 1$. Avoid $W/L \ll 1$ or $\gg 1$.	Low W/L (e.g., Design 1.b or 2.b) → (i) The largest scatter in metering volume variation. (ii) Susceptible to incomplete filling or metering.
B. Capillary length λ_σ vs. chamber dimensions	DO NOT operate in regimes where $\lambda_\sigma \approx W, H$ (e.g., low rotational speeds when chamber designed with $W \to H$).	When λ_σ becomes comparable to width W and depth H→ Larger interface curvature and greater susceptibility to volume variation
C. Rotational-speed independence	DO set speed high enough to suppress the capillary retention $H/\lambda_\sigma > 1$. DO NOT rely on speed alone to correct geometric under-/over-metering→ Centrifugal acceleration takes the rotational radius into account.	Rotational speed affects interface curvature; limited direct influence on metered volume under tested condition.
D. Inlet volume influence	DO keep the inlet volume variation small for stable metering.	ANOVA: inlet volume influences metering significantly in configuration *1*.

Table 2: Configuration-specific design rules based on experimentally observed behavior.

Configuration	Guideline (Prescriptive DO/DO NOT)	Rationale
Configuration *1*	DO keep the wall separating the metering and waste chambers sufficiently thin.	The thicker wall increases the effective chamber width when meniscus rises above the wall; $W \rightarrow W + d$, amplifies the volume variation $\Delta V \approx (W + d)H\lambda_\sigma$
	DO include a nose feature for reliable filling of chambers with narrow entrances.	Nose feature ensures void-free filling but delays liquid-tail removal → longer metering
	DO optimize the nose dimensions to minimize residual liquid.	When characteristic nose dimension ≈ λ_σ, capillary forces dominate → Residual trapped volume.
Configuration *2*	DO operate at conditions where the liquid height in the waste channel satisfies $\Delta h > \Delta h_{\max}$	Liquid plug in the waste channel persists when $\Delta h < \Delta h_{\max}$ and causes residual liquid
	DO keep chamber aspect ratio $W/H \approx 1$ when $V_{\text{inlet}} / V_{\text{chamber}} = \mathcal{O}(1)$.	Large W/L chamber (e.g., Design 2.d) reduces pressure head when inlet volume is comparable to metering volume → Incomplete metering
Cartesian vs. Cylindrical Layouts Tested for Configuration 2	DO prefer cylindrical layout when identical metering chambers are required.	Misalignment in Cartesian layout causes systematic left/right volume imbalance based on the waste channel position.
	DO NOT use identical left/right (L/R) chambers in Cartesian layout without geometric compensation.	Chambers on "waste-side" produce smaller metering volumes and vice versa. The relative error can be estimated as: $\frac{\lvert\Delta V\rvert}{V} \approx \frac{W\tan(\alpha)}{2L}$. For the present geometry, the above expression predicts $\Delta V/V \approx 8.8\%$, consistent with the measured inter-chamber CV (~12%). Compensation reduces layout-induced bias.
	DO orient the smallest chamber dimension radially (and the largest dimension along rotation axis.	Ensures that the meniscus spans the largest dimension perpendicular to centrifugal acceleration, improving metering uniformity.

Although the present study focuses on single-chamber metering, the investigated configurations serve as building blocks for multi-chamber architectures. Configuration *1* enables parallel generation of multiple sub-volumes (e.g., dispensing and mixing multi reagents [24,38,46]), whereas Configuration *2* supports precise one-to-one aliquoting for controlled dosing or sample preparation [8,30].

Unlike earlier centrifugal metering studies that focused on closed centrifugo-pneumatic chambers with volume definition governed by trapped air compression (e.g., Mark et al., Schwemmer et al. [31,33]), the design rules summarized here address open and overflow-based metering architectures, where volume selection is controlled by the interplay of capillary forces, centrifugal acceleration, and residual liquid retention. In contrast to application-specific investigations such as Lutz et al. [32], which optimized metering for a fixed cartridge and assay workflow, the present tables distill geometry- and physics-based constraints that remain valid across inlet volumes, rotational speeds, layouts, and fabrication approaches.

The framework developed here is directly relevant to the design of LOAD platforms used in biochemical and diagnostic workflows. In many centrifugal microfluidic assays—including enzymatic reactions, immunoassays, and multiplexed sample preparation—accurate aliquoting is required to distribute samples or reagents into controlled sub-volumes prior to downstream processing. Variations in metered volume can propagate through the workflow and affect reagent concentrations, reaction kinetics, and ultimately analytical accuracy.

The applicability of the design rules depends on the physical properties of the working fluid. The experiments presented in this work were conducted using water as a model liquid in order to isolate the influence of geometry and operating conditions on the metering behavior. Water provides well-characterized physical properties and allows controlled evaluation of the capillary–centrifugal interactions governing the liquid–air interface. Fluids used in practical applications may exhibit different surface tension and viscosity. Advancing and receding contact angles may also vary with both the fluids and the materials used in device fabrication. These properties can modify the quantitative thresholds reported here, such as the capillary length, the liquid-plug retention conditions, and the centrifugal acceleration required for reliable metering. Nevertheless, the physical framework established in this work—based on the balance between centrifugal and capillary forces and the geometric scaling of the metering chambers—remains broadly applicable to other liquids except for strongly wetting liquids (very small contact angles), such as certain oils, where capillary wicking is expected to dominate.

4 Conclusions

This study presented a systematic investigation of the metering function in centrifugal microfluidic systems, with a focus on how design parameters, dynamic operational conditions, and geometrical layouts influence the metering performance. Leveraging a flexible Chip-on-a-Disk (COAD) platform, we conducted extensive experiments across two distinct microfluidic configurations, each comprising five design variants, under varying conditions of chamber dimensions, rotational speed, and inlet volume. We demonstrated that deviations from ideal metering—such as over- or under-metering—were significantly influenced by these design variations. Additionally, variations in inlet volume were shown to impact performance when targeting metered volumes below 1 µL. Experimental results were rationalized by physical arguments. In particular, we identified the threshold on centrifugal acceleration above which parasitic liquid plugs within the microfluidic features connected to the metering chamber could be effectively removed. The smallest dimension of the microfluidic geometry or unit was found to be the most critical design parameter contributing to liquid retention and plug formation. This suggests that optimizing geometries with respect to their smallest dimension can facilitate plug removal at lower rotational speeds. Our analysis also highlighted the importance of the fabrication process in determining surface wettability, which plays a key role in minimizing the trapping of liquid residues and the formation of rivulet flows in specific configurations.

Furthermore, we evaluated the effect of in-plane circuit layout (Cartesian vs. cylindrical). Cartesian layouts introduced angular deviations of the centrifugal force, leading to systematic discrepancies in

metered volumes across circuits. While these variations were reproducible, they necessitate compensatory design adjustments—such as modifying chamber geometries based on positional bias—to achieve uniform volume selection. In contrast, cylindrical layouts yielded more uniform and precise metering, benefiting from symmetric centrifugal alignment.

These findings provide practical insights for improving the metering reliability of centrifugal platforms, particularly for applications requiring high precision and integration of complex workflows. This work contributes toward the development of predictive design guidelines and robust fluidic architectures for next generation of LOAD systems in diagnostics, biochemistry, and sample preparation.

Author Contributions

Ali Gholizadeh: Conceptualization, methodology, software, data curation, validation, formal analysis, investigation, writing – original Draft, Writing – critical Review & Editing, and visualization.

Oliver Verlaine: Conceptualization, methodology, software, and visualization.

Tristan Gilet: Conceptualization, software, validation, resources, writing – critical review & editing (Commentary or Revision), and supervision.

Acknowledgements

The authors thank Denis Vandormael (Sirris) for manufacturing the microfluidic chips, and Gabriel Mazzucchelli, the project coordinator, for his insightful discussions on the application of this work. This research was funded by the Wallonia Public Service (SPW) through the Win2Wal grant 2010126 (ChipOmics).

References

[1] J. Kim, M. Johnson, P. Hill, B.K. Gale, Microfluidic sample preparation: Cell lysis and nucleic acid purification, Integrative Biology 1 (2009) 574–586. https://doi.org/10.1039/b905844c.

[2] F. Cui, M. Rhee, A. Singh, A. Tripathi, Microfluidic Sample Preparation for Medical Diagnostics, Annu. Rev. Biomed. Eng. 17 (2015) 267–286. https://doi.org/10.1146/annurev-bioeng-071114-040538.

[3] A. Dehghan, M.J. Kiani, A. Gholizadeh, J. Aminizadeh, A. Rahi, I. Zare, E. Pishbin, H. Heli, Electrochemical genosensors on-a-chip: Applications in early diagnosis of pathogens, Sensors and Actuators Reports 9 (2025) 100335. https://doi.org/10.1016/J.SNR.2025.100335.

[4] H. Yuan, Z. Miao, C. Wan, J. Wang, J. Liu, Y. Li, Y. Xiao, P. Chen, B.F. Liu, Recent advances in centrifugal microfluidics for point-of-care testing, Lab Chip 25 (2025) 1015–1046. https://doi.org/10.1039/d4lc00779d.

[5] M. Madou, J. Zoval, G. Jia, H. Kido, J. Kim, N. Kim, Lab on a Cd, Annu. Rev. Biomed. Eng. 8 (2006) 601–628. https://doi.org/10.1146/annurev.bioeng.8.061505.095758.

[6] D. Mark, S. Haeberle, G. Roth, F. von Stetten, R. Zengerle, Microfluidic lab-on-a-chip platforms: requirements, characteristics and applications., Chem. Soc. Rev. 39 (2010) 1153–82. https://doi.org/10.1039/b820557b.

[7] S. Haeberle, R. Zengerle, Microfluidic platforms for lab-on-a-chip applications, Lab Chip 7 (2007) 1094–1110. https://doi.org/10.1039/b706364b.

[8] A. Gholizadeh, G. Mazzucchelli, T. Gilet, Flipping: A Valve-Free Strategy to Control Fluid Flow in Centrifugal Microfluidic Systems, Sens. Actuators B Chem. 412 (2024). https://doi.org/10.1016/j.snb.2024.135778.

[9] R. Gorkin, J. Park, J. Siegrist, M. Amasia, B.S. Lee, J.-M. Park, J. Kim, H. Kim, M. Madou, Y.-K. Cho, Centrifugal microfluidics for biomedical applications, Lab Chip 10 (2010) 1758. https://doi.org/10.1039/b924109d.

[10] S.O. Sundberg, C.T. Wittwer, C. Gao, B.K. Gale, Spinning disk platform for microfluidic digital polymerase chain reaction, Anal. Chem. 82 (2010) 1546–1550. https://doi.org/10.1021/ac902398c.

[11] C.T. Schembri, T.L. Burd, A.R. Kopf-Sill, L.R. Shea, B. Braynin, Centrifugation and capillarity integrated into a multiple analyte whole blood analyser, Journal of Automatic Chemistry 17 (1995) 99–104. https://doi.org/10.1155/S1463924695000174,.

[12] A. Dehghan, A. Gholizadeh, M. Navidbakhsh, H. Sadeghi, E. Pishbin, Integrated microfluidic system for efficient DNA extraction using on-disk magnetic stirrer micromixer, Sens. Actuators B Chem. 351 (2022). https://doi.org/10.1016/j.snb.2021.130919.

[13] J.N. Kuo, X.F. Chen, Plasma separation and preparation on centrifugal microfluidic disk for blood assays, Microsystem Technologies 21 (2015) 2485–2494. https://doi.org/10.1007/S00542-015-2408-8/FIGURES/10.

[14] S. Peshin, M. Madou, L. Kulinsky, Microvalves for Applications in Centrifugal Microfluidics, Sensors 22 (2022). https://doi.org/10.3390/s22228955.

[15] T.H. Kim, J. Park, C.J. Kim, Y.K. Cho, Fully integrated lab-on-a-disc for nucleic acid analysis of food-borne pathogens, Anal. Chem. 86 (2014) 3841–3848. https://doi.org/10.1021/ac403971h.

[16] O. Strohmeier, S. Laßmann, B. Riedel, D. Mark, G. Roth, M. Werner, R. Zengerle, F. von Stetten, Multiplex genotyping of KRAS point mutations in tumor cell DNA by allele-specific real-time PCR on a centrifugal microfluidic disk segment, Microchimica Acta 181 (2014) 1681–1688. https://doi.org/10.1007/s00604-013-1099-z.

[17] S. Wang, X. Zhang, C. Ma, S. Yan, D. Inglis, S. Feng, A Review of Capillary Pressure Control Valves in Microfluidics, Biosensors 2021, Vol. 11, Page 405 11 (2021) 405. https://doi.org/10.3390/BIOS11100405.

[18] Y. Zhu, Y. Chen, Y. Xu, Interruptible siphon valving for centrifugal microfluidic platforms, Sens. Actuators B Chem. 276 (2018) 313–321. https://doi.org/10.1016/j.snb.2018.08.123.

[19] Q. Yan, S. Xuan, X. Ruan, J. Wu, X. Gong, Magnetically controllable generation of ferrofluid droplets, Microfluid. Nanofluidics 19 (2015) 1377–1384. https://doi.org/10.1007/s10404-015-1652-7.

[20] D.J. Kinahan, S.M. Kearney, N. Dimov, M.T. Glynn, J. Ducrée, Event-triggered logical flow control for comprehensive process integration of multi-step assays on centrifugal microfluidic platforms, Lab Chip 14 (2014) 2249–2258. https://doi.org/10.1039/c4lc00380b.

[21] D.C. Duffy, H.L. Gillis, J. Lin, N.F. Sheppard, G.J. Kellogg, Microfabricated Centrifugal Microfluidic Systems: Characterization and Multiple Enzymatic Assays, Anal. Chem. 71 (1999) 4669–4678. https://doi.org/10.1021/ac990682c.

[22] M. Tang, G. Wang, S.K. Kong, H.P. Ho, A Review of Biomedical Centrifugal Microfluidic Platforms, Micromachines 2016, Vol. 7, Page 26 7 (2016) 26. https://doi.org/10.3390/mi7020026.

[23] T.H. Kim, C.J. Kim, Y. Kim, Y.K. Cho, Centrifugal microfluidic system for a fully automated N-fold serial dilution, Sens. Actuators B Chem. 256 (2018) 310–317. https://doi.org/10.1016/J.SNB.2017.10.096.

[24] Y. Xiao, S. Li, Z. Pang, C. Wan, L. Li, H. Yuan, X. Hong, W. Du, X. Feng, Y. Li, P. Chen, B.F. Liu, Multi-reagents dispensing centrifugal microfluidics for point-of-care testing, Biosens. Bioelectron. 206 (2022). https://doi.org/10.1016/j.bios.2022.114130.

[25] M. La, S.M. Park, D.S. Kim, Centrifugal multiplexing fixed-volume dispenser on a plastic lab-on-a-disk for parallel biochemical single-end-point assays, Biomicrofluidics 9 (2015). https://doi.org/10.1063/1.4905940/892769.

[26] J. Park, V. Sunkara, T.H. Kim, H. Hwang, Y.K. Cho, Lab-on-a-disc for fully integrated multiplex immunoassays, Anal. Chem. 84 (2012) 2133–2140. https://doi.org/10.1021/ac203163u.

[27] H. Van Nguyen, V.M. Phan, T.S. Seo, High-throughput centrifugal microfluidic platform for multiplex respiratory virus diagnostics, Sens. Actuators B Chem. 399 (2024) 134771. https://doi.org/10.1016/J.SNB.2023.134771.

[28] A. Kloke, A.R. Fiebach, S. Zhang, L. Drechsel, S. Niekrawietz, M.M. Hoehl, R. Kneusel, K. Panthel, J. Steigert, F. Von Stetten, R. Zengerle, N. Paust, The LabTube-a novel microfluidic platform for assay automation in laboratory centrifuges, Lab Chip 14 (2014) 1527–1537. https://doi.org/10.1039/c3lc51261d.

[29] A. Gholizadeh, G. Mazzucchelli, C. Kune, T. Gilet, Fluidic Unit for Discrete Element Trapping, WO2024175769A1, 2024. https://hdl.handle.net/2268/321611.

[30] A. Gholizadeh, G. Mazzucchelli, A. Amoroso, T. Gilet, Modular Centrifugal Microfluidics for Sample Preparation, Anal. Chem. 97 (2025) 12070–12079. https://doi.org/10.1021/ACS.ANALCHEM.5C00076/ASSET/IMAGES/LARGE/AC5C00076_0008.JPEG.

[31] D. Mark, P. Weber, S. Lutz, M. Focke, R. Zengerle, F. von Stetten, Aliquoting on the centrifugal microfluidic platform based on centrifugo-pneumatic valves, Microfluid. Nanofluidics 10 (2011) 1279–1288. https://doi.org/10.1007/s10404-010-0759-0.

[32] S. Lutz, E. Lopez-Calle, P. Espindola, C. Boehm, T. Brueckner, J. Spinke, M. Marcinowski, T. Keller, A. Tgetgel, N. Herbert, T. Fischer, E. Beiersdorf, A fully integrated microfluidic platform for highly sensitive analysis of immunochemical parameters, Analyst 142 (2017) 4206–4214. https://doi.org/10.1039/C7AN00547D.

[33] F. Schwemmer, T. Hutzenlaub, D. Buselmeier, N. Paust, F. Von Stetten, D. Mark, R. Zengerle, D. Kosse, Centrifugo-pneumatic multi-liquid aliquoting - Parallel aliquoting and combination of multiple liquids in centrifugal microfluidics, Lab Chip 15 (2015) 3250–3258. https://doi.org/10.1039/c5lc00513b.

[34] J. Ducrée, S. Haeberle, S. Lutz, S. Pausch, F. Von Stetten, R. Zengerle, The centrifugal microfluidic Bio-Disk platform, Journal of Micromechanics and Microengineering 17 (2007). https://doi.org/10.1088/0960-1317/17/7/S07.

[35] M. Madadelahi, L.F. Acosta-Soto, S. Hosseini, S.O. Martinez-Chapa, M.J. Madou, Mathematical modeling and computational analysis of centrifugal microfluidic platforms: a review, Lab Chip 20 (2020) 1318–1357. https://doi.org/10.1039/c9lc00775j.

[36] J.L. Garcia-Cordero, L. Basabe-Desmonts, J. Ducrée, A.J. Ricco, Liquid recirculation in microfluidic channels by the interplay of capillary and centrifugal forces, Microfluid. Nanofluidics 9 (2010) 695–703. https://doi.org/10.1007/S10404-010-0585-4/FIGURES/6.

[37] J. Steigert, M. Grumann, T. Brenner, L. Riegger, J. Harter, R. Zengerle, J. Ducrée, Fully integrated whole blood testing by real-time absorption measurement on a centrifugal platform, Lab Chip 6 (2006) 1040–1044. https://doi.org/10.1039/b607051p.

[38] O. Verlaine, A. Amoroso, M. Remy, S. Wautier, R. Robiette, B. Joris, T. Gilet, Enzymatic assay in a lab-on-a-disk format to measure free piperacillin concentration in serum, Biomedical Microdevices 2026 28:2 28 (2026) 24-. https://doi.org/10.1007/s10544-026-00807-z.

[39] D. Podbiel, R. Zengerle, J. Hoffmann, An analytical model for void-free priming of microcavities, Microfluid. Nanofluidics 24 (2020) 1–10. https://doi.org/10.1007/S10404-020-2318-7/FIGURES/5.

[40] P.-G. de Gennes, F. Brochard-Wyart, D. Quéré, Capillarity and Wetting Phenomena, Springer New York, 2004. https://doi.org/10.1007/978-0-387-21656-0.

[41] P. Concus, R. Finn, ON THE BEHAVIOR OF A CAPILLARY SURFACE IN A WEDGE, Proceedings of the National Academy of Sciences 63 (1969) 292–299. https://doi.org/10.1073/PNAS.63.2.292,.

[42] N. Kubochkin, T. Gambaryan-Roisman, Capillary-driven flow in corner geometries, Curr. Opin. Colloid Interface Sci. 59 (2022) 101575. https://doi.org/10.1016/J.COCIS.2022.101575.

[43] G. Croce, N. Suzzi, Instability of a Film Falling Down a Bounded Plate and Its Application to Structured Packing, Fluids 2025, Vol. 10, Page 30 10 (2025) 30. https://doi.org/10.3390/FLUIDS10020030.

[44] H. Cho, H.Y. Kim, J.Y. Kang, T.S. Kim, How the capillary burst microvalve works, J. Colloid Interface Sci. 306 (2007) 379–385. https://doi.org/10.1016/j.jcis.2006.10.077.

[45] A. Gholizadeh, G. Mazzucchelli, A. Amoroso, T. Gilet, WellOmics: A Modular Microfluidic Well Plate for Versatile Sample Preparation, Demonstrated by an Enzymatic Assay, 2025 MicroTAS Book of Abstracts (2025). https://doi.org/10.70477/EBIB6691.

[46] A. Gholizadeh, G. Mazzucchelli, C. Kune, T. Gilet, Fluidic Device for Metering and Dispensing a Plurality of Samples, WO2025176316, 2025.